applied optics

Single-step fabrication of thin-film linear variable bandpass filters based on metal–insulator–metal geometry

Calum Williams,* Girish Rughoobur, Andrew J. Flewitt, and Timothy D. Wilkinson

Electrical Engineering Division, Department of Engineering, University of Cambridge, 9 JJ Thomson Avenue, Cambridge CB3 0FA, UK
*Corresponding author: cw507@cam.ac.uk

A single-step fabrication method is presented for ultra-thin, linearly variable optical bandpass filters (LVBFs) based on a metal–insulator–metal arrangement using modified evaporation deposition techniques. This alternate process methodology offers reduced complexity and cost in comparison to conventional techniques for fabricating LVBFs. We are able to achieve linear variation of insulator thickness across a sample, by adjusting the geometrical parameters of a typical physical vapor deposition process. We demonstrate LVBFs with spectral selectivity from 400 to 850 nm based on Ag (25 nm) and MgF_2 (75–250 nm). Maximum spectral transmittance is measured at ∼70% with a Q-factor of ∼20.

1. INTRODUCTION

Optical transmission filters, specifically linear variable bandpass filters (LVBFs), are crucial optical elements in a number of different applications including astronomy and hyper-spectral imaging [1]. The cost of LVBFs is relatively expensive for what are commonly Fabry–Perot (FP) etalons with a 1D thickness variation profile (cavity). Conventional LVBF fabrication processes include reflow of photographically patterned layers of resist [2,3], gray-scale lithography [4], and mechanically moving multiple graded masks [5]. However, these techniques suffer drawbacks including high cost, complexity, and processing time. Alternatives include holographic color filters [6], but these suffer from inherent diffraction orders and, again, require expensive lithographic processes. More recently, plasmonic-enhanced optical elements have been investigated [7–12], yet they inherently suffer damping (loss) mechanisms and likewise require lithographic processes.

Metal–insulator–metal (MIM) geometries have been extensively studied in the literature and have been shown to offer a range of attractive optical characteristics for applications including super absorbers and color filters [9,13–18]. Their reduced angular dependence, sub-wavelength thickness, reduced fabrication complexity, and non-structured and continuous ultra-thin nature make them interesting candidates for low-cost LVBFs.

When the electric field of light interacts with a MIM cavity, the resonant FP-mode associated with the dielectric cavity is terminated by two ultra-thin metallic layers, which act as partially reflective mirrors. The mirror thickness is less than or comparable to the metal skin depth, enabling transmission into the cavity. At resonance, the field is highly concentrated in the central region of the cavity. For a back-mirror thickness greater than the skin depth, perfect absorption can be achieved, whereas for thickness similar to the top mirror, transmission filtering is possible. By adjusting the mirror thicknesses, optimal coupling into the cavity mode for a particular wavelength can be achieved [14,15,18]. In this paper, using fabrication methodology based on the modification of conventional metal evaporation techniques, we demonstrate LVBFs based on ultra-thin-film MIM cavities at first-order resonance, which include a thin (25 nm) top–bottom metallic (Ag) layer coupled to a dielectric cavity composed of transparent MgF_2 (75–250 nm). Through this thickness variation, spectral selectivity from blue-NIR is achieved in a single device. Figure 1 highlights the concept, whereby the LVBF exhibits a spatially varying (1D) dielectric cavity [Figs. 1(a) and 1(c)] terminated by two metallic mirrors, in comparison to a single-wavelength device [Fig. 1(b)].
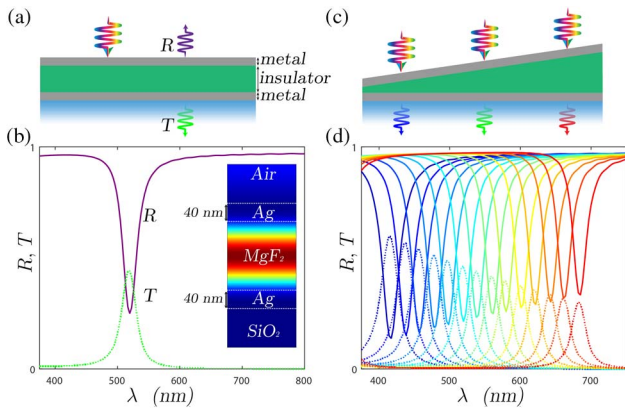
Fig. 1. MIM filter design. (a) Constant cavity thickness MIM LVBF composed of Ag (40 nm) and MgF_2 dielectric with FDTD simulation results in (b) the E-field profile at first-order resonance (inset). (c) MIM LVBF with gradient dielectric. (d) Simulated spectral properties as the position of observation on the sample changes (blue–red = dielectric thickness increase).
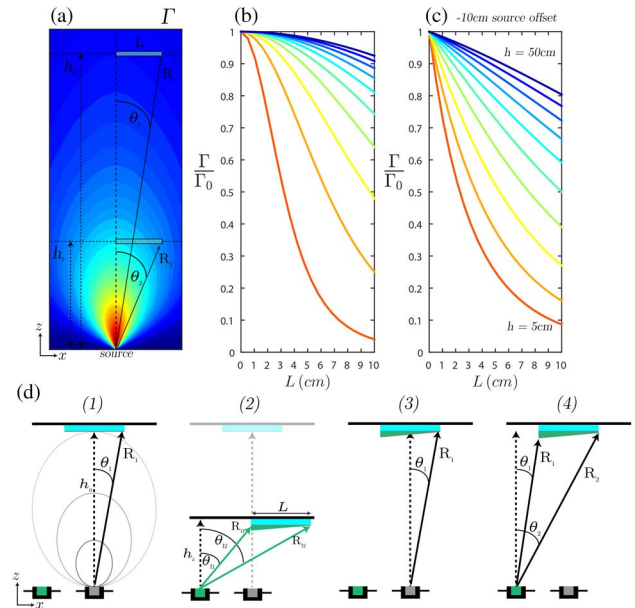

Fig. 2. Evaporation principles. (a) Deposition rate profile of a non-ideal source ($n = 1.5$). (b) Normalized deposition as a function of position along sample (on-axis) as substrate height varies. (c) Same as (b) but with lateral offset. (d) Fabrication process flow.

2. DESIGN

A. Fabrication

To obtain a device whereby the thickness profile of deposited material is continually varying (linearly or otherwise) presents a fabrication difficulty. Most process steps, either etching or physical/chemical vapor deposition, generally act uniformly across a sample [19]. Furthermore, conventional techniques for fabricating LVBFs [2–5,20] require additional masks or lithographic steps for resist reflow. For a typical physical vapor deposition evaporation process, such as thermal evaporation, at a typical chamber base pressure of 10^{-6} mbar, the mean-free path of molecular vapor is much larger than the typical chamber length ($\sim$50 cm); thus a 'line-of-sight' deposition can be approximated. Hence, the deposition rate (nm $\cdot$ s^{-1}), Γ, of an evaporated source with finite surface area can be written as

$$\Gamma \propto \cos^n(\theta_i) R_i^{-2}, \quad \text{(1)}$$

where n is a decimal or an integer describing emission profile, whereby for $n > 1$, non-ideal (increasing anisotropy) emission behavior is described [21]. R is the source-sample distance. Figures 2(a) and 2(b) show how the deposition rate (non-ideal source, with $n = 1.5$) varies as a function of distance from the source (on-axis). This value is an estimate based on the geometry of the apparatus and previous experimental work. Normally, to achieve uniform thickness, the sample is placed far enough away from the source in order to obtain similar deposition rates across the sample; i.e., for a sample of finite length, deposition uniformity increases as R increases.

By controlling the position of the sample and source within the chamber, and keeping a relatively low deposition rate in order to minimize delamination effects, the deposition rate across a sample can be spatially tailored, and hence a near-linear gradient distribution of source material can be deposited by calculating the correct geometry parameters to form linear variable devices. Figures 2(c) and 2(d) show how, by laterally offsetting a source, a "near-linear" thickness profile is readily obtainable. In Fig. 2(d), the steps are as follows: (1) on-central-axis deposition

maximizes separation to obtain a uniform deposition rate for the first metal mirror; (2) the sample is brought closer to the source, the source is negatively offset, and now a spatially variant deposition profile across the sample occurs; (3) same process as (1) for the second metal mirror; (4) an encapsulation layer is deposited to prevent degradation. Moreover, through the adjustment of the "source-function," a variety of thickness profiles, over varying length scales, can be achieved.

For this study, to obtain the near-linear variation of the insulator across a sample with length <10 cm, the concept is to reduce R and spatially offset both the sample and source material. Keeping the metal source close to on-sample-axis, the dielectric laterally offset, and the sample offset laterally in the opposite direction will ensure near uniform metal thickness and linearly variant dielectric thickness. The sample holder distance (h) is chosen to be $\sim$7.5 cm with lateral offset $\sim$10 cm. Molybdenum evaporation boats with Ag wire (99.9%) and MgF_2 (99.9%) optical grade evaporation pieces and glass slides are used. MgF_2 is chosen due to its low melting point, low cost, and optical properties—specifically, its relatively flat dispersion across 400–850 nm. The glass (thickness 0.7 mm) is cleaved, cleaned in subsequent ultrasonic baths of acetone and isopropyl alcohol (IPA), blow dried with N_2, and then dehydrated at 360°C for 10 min. Deposition in the thermal evaporator is performed at a base pressure of $\sim$2 × 10^{-6} mbar and with film thickness monitored (quartz crystal monitor) deposition at 0.1 nm $\cdot$ s^{-1}, for both Ag and MgF_2. The monitor is located at a fixed position approximately 10 cm from the central axis of the chamber.

It is important to note some materials considerations, specifically the integrity of the thin films. Generally, Ag adheres poorly to glass, and the low mechanical stability between Ag

and MgF$_2$ means that for future larger-scale fabrication, a thin coating (Ti/Cr) to promote adhesion would be necessary. MgF$_2$ is used here; however, a range of dielectrics can be used that are more chemically suitable for larger-scale processing. To obtain good quality, high packing density (hence low permeability to water vapor) thin films, thermal evaporation of MgF$_2$ is best performed with a raised substrate temperature ($>200°C$) and Ag with a cooler substrate (else sputtering techniques are possible). For this proof-of-concept study, substrate temperature control and additional adhesion layers were not utilized, and hence the devices here are potentially vulnerable to degradation over their lifespan. However, both problems are relatively straightforward to solve for future fabrication (and done so at an industrial scale), and a pure materials optimization is beyond the scope of this work.

B. Simulation

Figure 3 shows the compiled results from finite-difference time-domain (FDTD) simulations [22] of a range of MIM devices using Ag:MgF$_2$:Ag. Ag is chosen over Au based on the inherent interband electron transitions affecting the optical behavior of Au at shorter wavelengths and subsequently the more linear response of Ag across the entirety of the spectrum range of interest. The transmission maxima, reflection minima, and Q-factors ($\lambda/\Delta\lambda$), with respective wavelengths, taken from a range of simulations, are plotted. Simulations are performed using a mesh size of 0.5 nm, broadband plane-wave input, periodic boundary conditions, and a range of device geometries. Transmission and reflection values are calculated from power monitors positioned on either side of the structure. Complex dispersive material models are used for Ag (CRC), SiO$_2$ (Palik),

and a real, non-dispersive refractive index of 1.38 for MgF$_2$. Figures 3(a)–3(c) illustrate the linear behavior of the transmission peak as a function of dielectric and Ag mirror thickness, where the size of the data point indicates the associated transmission amplitude. The increase in dielectric thickness linearly red-shifts the cavity mode's spectral position, whereas metal thickness contributes to cavity finesse, as shown in Fig. 3. Generally, there is a trade-off between cavity finesse and transmission amplitude. From the simulation results, 25 nm of Ag is chosen as the top–bottom metallic layers in order to maximize transmission while maintaining spectral selectivity and high Q-factors. The spatial variation of MgF$_2$ is chosen to be 75–250 nm in order to obtain an operating wavelength range of ~400–850 nm. These characteristics are used for the plots in Fig. 3(c).

3. DEVICES

Characterization is performed using a BX-51 Olympus optical microscope (Halogen light source with IR filters removed), with 5–20× objectives, attached via 200 μm core optical fiber to a spectrometer (OceanOptics HR2000+). The optical results are normalized to the transmission and reflection through an equally thick glass slide and bulk-Ag mirror reference, respectively.

Figure 4 shows the reflection and transmission results of a range of separate color filter devices based on constant thickness layers of Ag (25 nm): MgF$_2$ (variation):Ag (25 nm) structures. The samples are placed at default chamber height, and multiple depositions are used to obtain varying dielectric thickness layers. The results here were to validate the initial MIM filter concept and ensure that the deposition, parameters, etc., were suitable to produce color filters.

The sample stage height is now reduced to (~7.5 cm), bringing the sample much closer to the source material, in order to achieve the maximum linear variation over the smallest sample length; however, for optimal linearity, the stage height should be greater. The sample is laterally offset (~10 cm), and the MgF$_2$ source boat is negatively offset (~6 cm—the maximum possible in our setup). The height is such that deposition
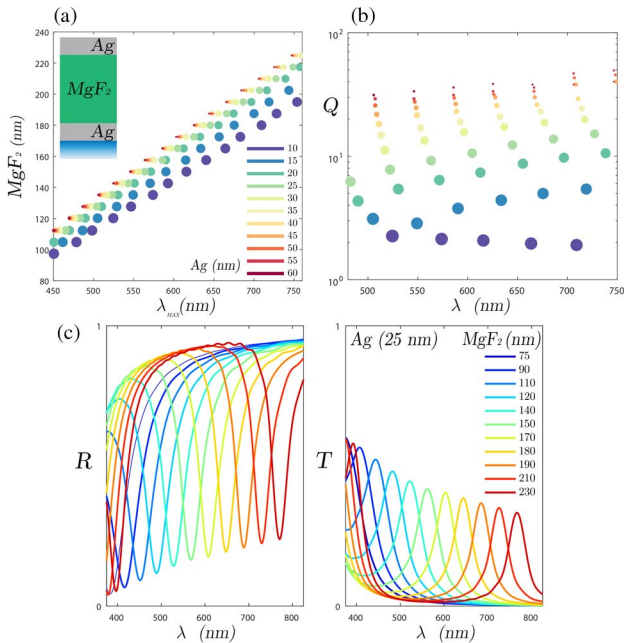

Fig. 3. FDTD simulation of MIM. (a) Peak transmission wavelengths as the dielectric and mirror thickness is varied. (b) Respective peak Q-factors; the size of the scatter points is proportional to transmission amplitude. (c) Reflection and transmission of MIM: Ag 25 nm mirrors with varying dielectric thickness.
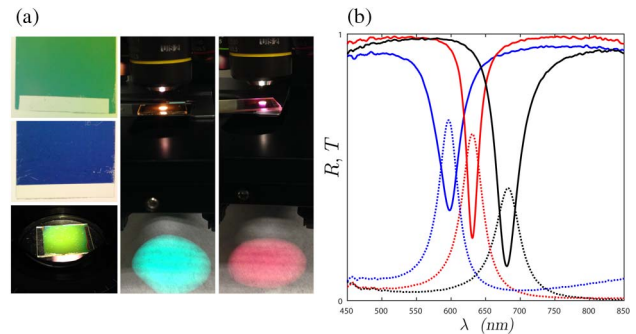

Fig. 4. Optical characterization results of single-wavelength filters. (a) Images of a range of samples with varying dielectric thicknesses showing the color filtering in transmission. (b) Three devices' reflection and transmission spectra: the MgF$_2$ thickness for each plotted spectrum (line-color: blue, red, black) is ~155, 172, and 189 nm, respectively. These are recorded from the quartz crystal thickness monitor.
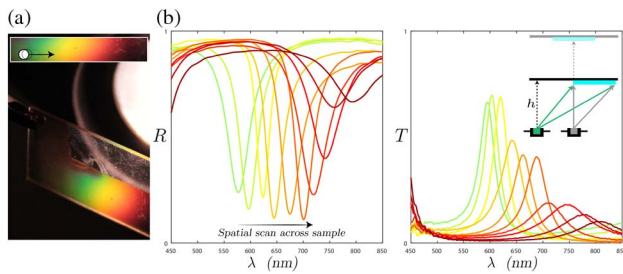
Fig. 5. Optical characterization results of MIM LVBF based on initial conditions. (a) Image taken of final device (length ~7.5 cm) in transmission. (b) Reflection and transmission results from spatially varying the objective collection spot linearly across the sample (thinner-thicker dielectric thickness). (Inset) Schematic of single-step deposition.

of MIM material is achieved without breaking vacuum for geometry adjustment. Figure 5 shows the reflection and transmission results of the LVBF obtained from this deposition. For deposition control, the concept in Fig. 2(c) is used to estimate the thickness across the sample stage based on thickness monitor output. Deviation from this model is due to the monitor position within the chamber (at an angle to source), finite source area (non-point-source-like behavior), and uncertainty in the exact value of the deposition parameter, n. Nevertheless, the top and bottom Ag mirror thicknesses were designed to be 25 nm and MgF$_2$, 75–250 nm. Figure 5(a) shows an image of the transmission of the sample, and Fig. 5(b) the spectra, as the objective (20×) collection spot is laterally moved; spectral selectivity of ~550–800 nm is observed. Peak transmission varies from ~70% – 10%, with a Q-factor variation of ~20 – 8. Intensity reduction and peak broadening as the collection spot is laterally moved across the sample (to longer wavelengths), in conjunction with the simulation results in Fig. 3, may suggest that the metal thickness also has a thickness variation across the sample that dampens the coupling into the cavity mode. This can be expected due to the fact that source(Ag)-sample central axes are different. Furthermore, full spectral range (blue-NIR) has not been achieved; thus the sample was in a sub-optimal position (lateral placement and or height from source). The deposition setup is subsequently adjusted to include the steps outlined in Figs. 2(d1)–2(d4). The bottom and top mirror metal is deposited at chamber height to reduce in-plane thickness variation. The dielectric is deposited with the source with negative lateral displacement; the sample has lateral displacement and reduced sample height once again. Additionally, an encapsulation layer (50 nm MgF$_2$) is deposited post-top-mirror layer. This reduces the degradation of the top metal in terms of environmental oxidation and offers increased mechanical stability, yet has few detrimental effects on the optical performance. Deposition of MIM material is now achieved with breaking vacuum for geometry modifications, and a larger glass substrate is used. Figure 6(a) shows the images of reflection and transmission of the sample on an optical bench, and Fig. 6(b) shows the measured spectra during lateral movement across the sample (20× objective), where (i) shows data taken with the device in the designed orientation and (ii) shows the same upside down (i.e., glass first). The observed operating wavelength range is ~400–850 nm. Peak transmission varies
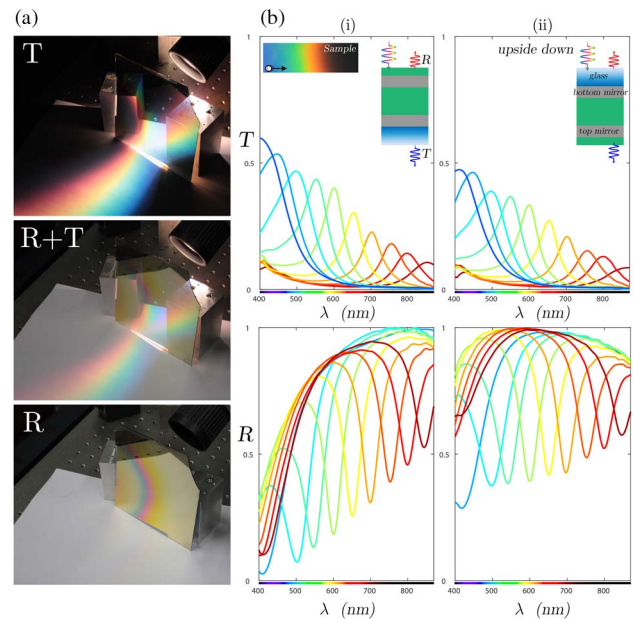

Fig. 6. Optical characterization results of Ag (25 nm): MgF$_2$ (range): Ag (25 nm) linearly variable filter. (a) Images of reflection and transmission of final device and (b) spectra of the device; inset shows an image of the filter in transmission at normal incidence.

from ~60% – 11% (i) and ~47% – 10% (ii), with a Q-factor variation of ~10 – 6 (i), and similar values in (ii). The image inset in (i) is of the filter in transmission, showing the range of colors filtered.

4. DISCUSSION AND COMPARISON

The transmission spectra in Fig. 6(b) are similar in nature to those of the simulations in Fig. 3(c) but with slightly reduced amplitudes and Q-factors. This can be attributed to non-optimal experimental deposition parameters. Furthermore, source offset (deposition angle variation) leads to a varying refractive index of MgF$_2$, which is not accounted for in the simulation work. Linearity is not completely matched to theoretical predictions, indicating a mismatch in the deposition parameter, n, of the actual system. The designed wavelength range is achieved; however, toward the shorter wavelength range we observe an additional absorption mechanism that is not present in Fig. 5(b), in the simulation results, or in the device in the reverse orientation [upside down: Fig. 6(b)(ii)]. In this deposition, vacuum was broken (exposed to atmospheric gases) to adjust the deposition geometry, and hence we speculate that this means that oxidation has occurred to the bottom mirror. Silver oxidizes rapidly when exposed to air, and silver oxide is known to be absorbing at wavelengths <500 nm [23]. Thus, this may help to explain the pronounced blue anomaly in Fig. 6(b)(i) to the effect that with a silver oxide surface layer, the larger extinction coefficient (blue part of the spectrum) for the back-mirror would mean similar operation for longer wavelengths but increased absorption at shorter wavelengths. An automated mechanical stage height and lateral adjustment for *in situ* geometrical adjustment, or a thin additional encapsulation layer, would help reduce the severity of this problem.

Through careful choice of geometry parameters, related to calibration data similar to Fig. 2, LVBFs with varying transmission functions can be achieved. However, a number of optimization techniques are required: through additional experiments, the exact emission value parameter used in the modeling can be determined, thus ensuring the thickness profile of the sample matches expectations. The final device does not exhibit a purely linear profile, and optimization of the boat shape, to tailor the plume profile, is necessary to produce greater linearity. In addition, as seen by the deposited material's circular distribution in Fig. 5(a), inherent in point-source-like evaporation techniques, the modification of the source function and source position optimization would allow for the tailoring of this final distribution. Further fabrication modifications should include real-time monitoring of the evaporation plume distribution (and how it evolves with time) through carefully designed positioning of precise thin-film monitors and *in situ* optical performance monitoring using angled-reflection measurements. Accounting for the refractive index variation of MgF_2 due to angled deposition in the simulation and performing ellipsometry to determine how the refractive index varies as a function of source offset. The devices exhibit unwanted higher-order harmonic modes, which can be suppressed with a multi-layer (multiple cavity) thin-film approach—also improving optimal transmittance and Q-factors. From a device integrity standpoint, as discussed earlier, substrate temperature control is critical to obtain densely packed, high-quality thin films and adhesion layers required for mechanical stability between Ag, glass, and MgF_2. Furthermore, the replacement of MgF_2 with another more suitable dielectric (better chemical and mechanical stability) is desirable; however, one then must consider using sputtering techniques due to the high temperatures required for evaporation of most dielectrics.

5. CONCLUSION

Existing techniques for fabricating LVBFs [2–5,20] require additional masks or lithography resist reflow. In this paper, we have shown an alternate technique for fabricating MIM LVBFs simply, with reasonable optical specifications, prior to any optimization of the process. By adjusting the spatial position of the sample and evaporation material within the chamber, deposition rate differences can be used in order to tailor linear varying thickness across glass samples. Ag (25 nm) and MgF_2 (75–250 nm) are used as the metal and dielectric materials, respectively, which give spectral sensitivity from 400 to 850 nm. Peak transmission varies from ∼70% – 10%, and a Q-factor ($\lambda/\Delta\lambda$) variation of ∼20 – 8 is observed. A number of optimization techniques have been outlined that are necessary in order to produce mechanically robust, optimal performance LVBFs using this approach. Commercial thin-film coating technologies commonly include thermal and e-beam evaporation; thus modification to include these modifications would be relatively straightforward.

REFERENCES

1. H. A. Macleod, *Thin-Film Optical Filters*, 3rd ed. (Institute of Physics, 1969).
2. A. Emadi, H. Wu, S. Grabarnik, G. De Graaf, K. Hedsten, P. Enoksson, J. Correia, and R. Wolffenbuttel, "Fabrication and characterization of IC-compatible linear variable optical filters with application in a micro-spectrometer," Sens. Actuators A **162**, 400–405 (2010).
3. N. P. Ayerden, G. de Graaf, and R. F. Wolffenbuttel, "Compact gas cell integrated with a linear variable optical filter," Opt. Express **24**, 2981–3002 (2016).
4. M. Fritze, J. Knecht, C. Bozler, C. Keast, J. Fijol, S. Jacobson, P. Keating, J. LeBlanc, E. Fike, B. Kessler, M. Frish, and C. Manolatou, "Fabrication of three-dimensional mode converters for silicon-based integrated optics," J. Vac. Sci. Technol. B **21**, 2897–2902 (2003).
5. A. Piegari, J. Bulir, and A. Krasilnikova Sytchkova, "Variable narrow-band transmission filters for spectrometry from space. 2. Fabrication process," Appl. Opt. **47**, C151–C156 (2008).
6. C. Moser, L. Ho, E. Maye, and F. Havermeyer, "Fabrication and applications of volume holographic optical filters in glass," J. Phys. D **41**, 224003 (2008).
7. T. Xu, Y.-K. Wu, X. Luo, and L. J. Guo, "Plasmonic nanoresonators for high-resolution colour filtering and spectral imaging," Nat. Commun. **1**, 59 (2010).
8. V. Raj Shrestha, S.-S. Lee, E.-S. Kim, and D.-Y. Choi, "Polarization-tuned dynamic color filters incorporating a dielectric-loaded aluminum nanowire array," Sci. Rep. **5**, 12450 (2015).
9. K. Aydin, V. E. Ferry, R. M. Briggs, and H. A. Atwater, "Broadband polarization-independent resonant light absorption using ultrathin plasmonic super absorbers," Nat. Commun. **2**, 517 (2011).
10. E. Laux, C. Genet, T. Skauli, and T. W. Ebbesen, "Plasmonic photon sorters for spectral and polarimetric imaging," Nat. Photonics **2**, 161–164 (2008).
11. C. Williams, Y. Montelongo, J. O. Tenorio-Pearl, A. Cabrero-Vilatela, S. Hofmann, W. I. Milne, and T. D. Wilkinson, "Engineered pixels using active plasmonic holograms with liquid crystals," Phys. Status Solidi RRL **9**, 125–129 (2015).
12. Y. Montelongo, J. O. Tenorio-Pearl, C. Williams, S. Zhang, W. I. Milne, and T. D. Wilkinson, "Plasmonic nanoparticle scattering for color holograms," Proc. Natl. Acad. Sci. **111**, 12679–12683 (2014).
13. B. Zeng, Y. Gao, and F. J. Bartoli, "Ultrathin nanostructured metals for highly transmissive plasmonic subtractive color filters," Sci. Rep. **3**, 1–9 (2013).
14. Z. Li, S. Butun, and K. Aydin, "Large-area, lithography-free super absorbers and color filters at visible frequencies using ultrathin metallic films," ACS Photon. **2**, 183–188 (2015).
15. G. Kajtár, M. Kafesaki, E. N. Economou, and C. M. Soukoulis, "Theoretical model of homogeneous metal-insulator-metal perfect multi-band absorbers for the visible spectrum," J. Phys. D **49**, 055104 (2016).
16. K. Diest, J. A. Dionne, M. Spain, and H. A. Atwater, "Tunable color filters based on metal-insulator-metal resonators," Nano Lett. **9**, 2579–2583 (2009).
17. M. A. Kats, R. Blanchard, P. Genevet, and F. Capasso, "Nanometre optical coatings based on strong interference effects in highly absorbing media," Nat. Mater. **12**, 20–24 (2012).
18. Y. Cui, Y. He, Y. Jin, F. Ding, L. Yang, Y. Ye, S. Zhong, Y. Lin, and S. He, "Plasmonic and metamaterial structures as electromagnetic absorbers," Laser Photon. Rev. **8**, 495–520 (2014).
19. S. Franssila, *Introduction to Microfabrication* (Wiley-Blackwell, 2010).
20. A. Emadi, H. Wu, S. Grabarnik, G. De Graaf, and R. F. Wolffenbuttel, "IC-compatible fabrication of linear variable optical filters for microspectrometer," Procedia Chem. **1**, 1143–1146 (2009).
21. M. Ohring, *Materials Science of Thin Films* (Academic, 1992).
22. Lumerical Solutions, Inc., http://www.lumerical.com/tcad-products/fdtd/.
23. G. S. S. Saini and S. K. Tripathi, *Thin Solid Films* (Elsevier, 1995).